Greater flood risks in response to slowdown of tropical cyclones over the coast of China

Yangchen Lai[a,b], Jianfeng Li[a,1], Xihui Gu[c,1], Yongqin David Chen[d,e], Dongdong Kong[c], Thian Yew Gan[f], Maofeng Liu[g], Qingquan Li[b], and Guofeng Wu[b]

[a]Department of Geography, Hong Kong Baptist University, Hong Kong, China; [b]Key Laboratory for Geo-Environmental Monitoring of Great Bay Area, Ministry of Natural Resources, Shenzhen University, Shenzhen 518060, China; [c]Department of Atmospheric Science, School of Environmental Studies, China University of Geosciences, Wuhan 430074, China; [d]School of Humanities and Social Science, The Chinese University of Hong Kong, Shenzhen 518172, China; [e]Department of Geography and Resource Management, The Chinese University of Hong Kong, Hong Kong, China; [f]Department of Civil and Environmental Engineering, University of Alberta, Edmonton, AB, T6G2W2, Canada; and [g]Department of Civil and Environmental Engineering, Princeton University, Princeton, NJ 08540

The total amount of rainfall associated with tropical cyclones (TCs) over a given region is proportional to rainfall intensity and the inverse of TC translation speed. Although the contributions of increase in rainfall intensity to larger total rainfall amounts have been extensively examined, observational evidence on impacts of the recently reported but still debated long-term slowdown of TCs on local total rainfall amounts is limited. Here, we find that both observations and the multimodel ensemble of Global Climate Model simulations show a significant slowdown of TCs (11% in observations and 10% in simulations, respectively) from 1961 to 2017 over the coast of China. Our analyses of long-term observations find a significant increase in the 90th percentile of TC-induced local rainfall totals and significant inverse relationships between TC translation speeds and local rainfall totals over the study period. The study also shows that TCs with lower translation speed and higher rainfall totals occurred more frequently after 1990 in the Pearl River Delta in southern China. Our probability analysis indicates that slow-moving TCs are more likely to generate heavy rainfall of higher total amounts than fast-moving TCs. Our findings suggest that slowdown of TCs tends to elevate local rainfall totals and thus impose greater flood risks at the regional scale.

tropical cyclones | translation speed | local rainfall totals | flood risks

T orrential rains induced by tropical cyclones (TCs) are a major trigger of catastrophic flood hazards in many coastal regions of the world (1–3). Flood risks in response to TC-induced rainfall at a given location are not only dependent on rainfall intensity but also the duration of TCs passing through the region (1, 4–7). Observations and numerical climate model simulations have both demonstrated that the maximum increase in TC-induced rainfall rate can reach about 10% per degree Celsius of warming, suggesting potentially greater flood threats associated with more intense TC-induced rainfall under climate warming (8–12). On the other hand, some devastating TCs in recent years were characterized with longer passage time (i.e., lower translation speed) through a region, resulting in greater rainfall totals. Hurricane Harvey stalled over Texas on 25–30 August 2017, leading to unprecedented flooding and severe damages with a 2,000-y local TC rainfall total (3, 13, 14). Super Typhoon Morakot, the deadliest typhoon in Taiwan in the recorded history, lingered over Taiwan for over 30 h on 8–11 August 2009 and brought about a record-breaking rainfall total of over 3,000 mm (4, 6). A global slowdown of TC translation speed in the best-track data has been recently reported (1, 15). However, compared to the increase of TC rainfall intensity with relatively higher confidence (10–12), the robustness and causative mechanisms of TC slowdown are still arguable (7, 15–19). This controversy is mainly caused by the inhomogeneity in the observed best-track data primarily due to the advancement in observation

techniques from the presatellite era to the postgeostationary-satellite era (16–18).

For an individual TC event, the local rainfall total is proportional to the rainfall intensity but inversely proportional to the translation speed (1, 4, 6, 7). There have been some event-based studies on the crucial role of slower translation speed and longer duration in increasing TC-induced rainfall [e.g., Hurricane Harvey and Typhoon Morakot (3, 4, 6, 13)]. However, over a long-term period, the responses of TC-induced rainfall to changes in TC characteristics appear highly stochastic and variable at various temporal and spatial scales (15, 20). The impacts of changes in TC translation speed on local rainfall totals in the long run have received much less attention compared to the effects of increased rainfall intensity (11, 12). Based on observations and simulations of eight Global Climate Models (GCMs) in the Coupled Model Intercomparison Project Phase 5 [CMIP5 (21)], we herein examine the changes of landfalling TC translation speed from 1961 to 2017, and evaluate to what extent such long-term changes have affected local rainfall totals over the coastal regions of China, one of the most TC-prone regions in the western North Pacific Ocean (*Methods* and *SI Appendix, Appendix A*). The coastal regions of China support nearly half of
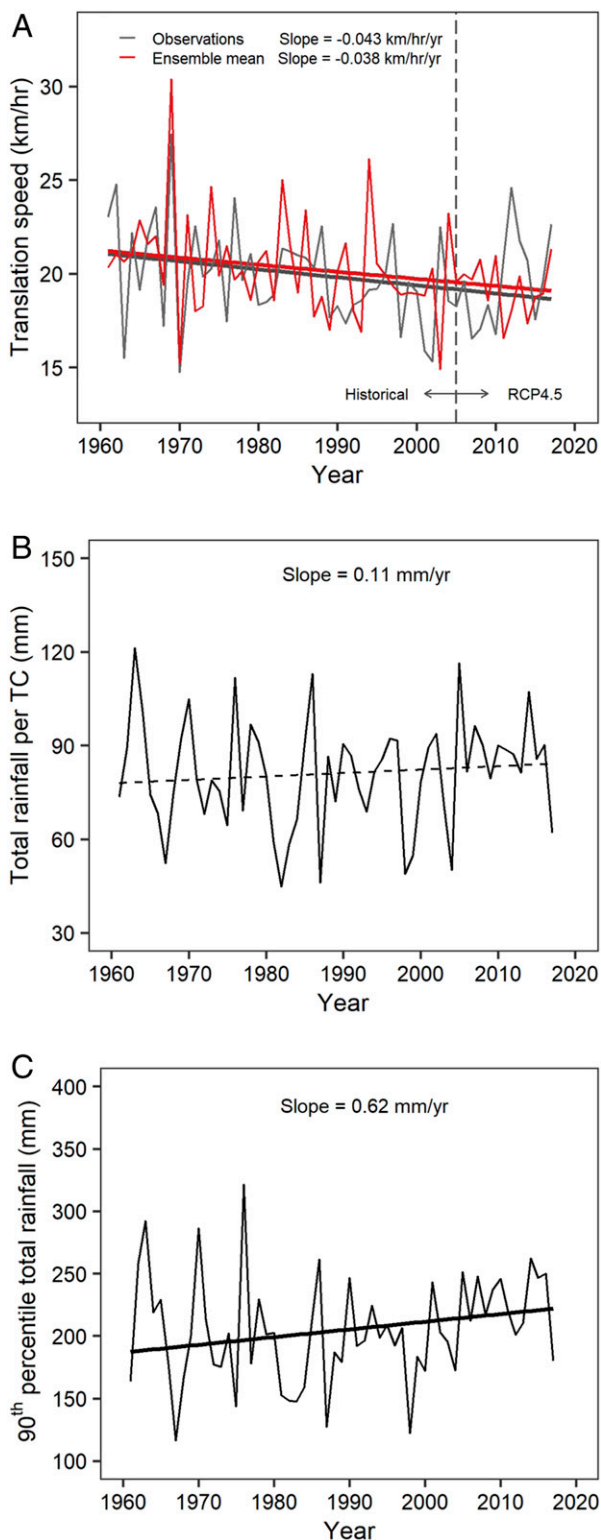
Fig. 1. Temporal evolution of annual-mean TC translation speed (km/h) and accumulated rainfall induced by TCs (mm) over the coastal areas of China from 1961 to 2017. (*A*) Annual-mean TC translation speed based on the best-track data (black) and the multimodel ensemble mean of CMIP5 GCMs (red). (*A*) The annual-mean TC translation speed in GCMs is extended to 2017 using the RCP4.5 scenario (right side of the vertical dashed line) from 1961 to 2005 under the historical scenario (left side of the vertical dashed line, refs. 45 and 46). The slowdown of TCs in GCMs is also significant in 1961–2005 under the historical scenario only without extension (*SI Appendix,* Appendix C and Fig. S3). (*B*) Annual-mean and (*C*) the 90th percentile of the areal-averaged

the country's population and a number of highly populous and developed metropolises, such as the Pearl River Delta and Yangtze River Delta, making the regions highly exposed and vulnerable to TC-related hazards (22, 23). Simulated and observational evidence is of great importance for an improved understanding of the compound effects of slow-moving TCs and intensification of TC-induced rainfall on local flood risks.

We find that both the best-track data and the CMIP5 GCM ensemble show significant and comparable decreases (−0.044 km/h per year or a total of −11% in observations and −0.038 km/h per year or a total of −10% in simulations, respectively) in the translation speed of TCs that made landfall along China's coastlines in 1961–2017 (Fig. 1*A*). As detailed in *Methods* and *SI Appendix,* Appendix B, the observed decreasing trend in this study should be less affected by the sampling bias in the best-track data compared to previous studies, because we exclude the TC track points located far away from the coast (15). Furthermore, the finding that the significant decreasing trends in the GCM-derived TC translation speed are comparable to those estimated from the best-track data adds more confidence in the slowdown of TCs over the past decades (1961–2017 under the historical and Representative Concentration Pathway 4.5 (RCP4.5) scenarios in Fig. 1*A*, and 1961–2005 under the historical scenario only in *SI Appendix,* Appendix C).

In our analyses of the impacts of TC slowdown on local rainfall totals, we first examine the long-term and overall changes in TC-induced rainfall totals during the study period. As shown in Fig. 1 *B* and *C*, both the annual mean and the 90th percentile of total rainfall per TC exhibited increasing trends over the period of 1961–2017. Moreover, the 90th percentile of the total rainfall increased significantly by 18% from 187 mm in 1961–223 mm in 2017. The increasing trends in TC-induced rainfall amounts are consistent with those reported in previous studies using different datasets or TC detection methods (24–26). Next, we analyze the correlations between TC translation speed and local rainfall total of individual TCs. Fig. 2 shows the general spatial pattern of negative Spearman correlations for TCs with rainfall intensities ≥ 30 mm/d, which confirms the inverse relationship between TC translation speeds and local rainfall totals. To further verify this pattern, we evaluate these negative correlations for TCs with rainfall intensities in other ranges and find that the pattern is consistent and the inverse relationships are even stronger for TCs causing more intense rainfall (*SI Appendix,* Appendix D). We obtain similar results in the analysis based on the Pearson correlation (*SI Appendix,* Appendix D). The above spatial patterns consistently indicate that the inverse relationships are statistically significant and tend to be stronger at more locations in southern China. Therefore, we select the highly populated and developed Pearl River Delta city region (see Fig. 2 for its location) as our focus to analyze how translation speed affects the local rainfall total of TC events generating rainfall of different intensities. The scatter plot in Fig. 3*A* exhibits the influence of TC translation speed in modulating local TC rainfall totals. The Spearman correlation coefficient reaches −0.53 for the TC events generating rainfall of more than 30 mm/d. Fig. 3*A* also shows that TC events with similar rainfall intensities produce higher rainfall total when the TC moves at a lower translation speed. It is evident that TC events with high rainfall intensity and low translation speed bring about the largest local rainfall totals (the scatter points in the upper left) and those with high translation speed generally produce less rainfall (the scatter points in the bottom right).

rainfall totals of TCs, respectively. In *A*, *B*, and *C*, solid straight line indicates the trend is significant at the 95% level based on the modified Mann–Kendall test, while dashed straight line means the trend is insignificant. Sen's slope is shown.
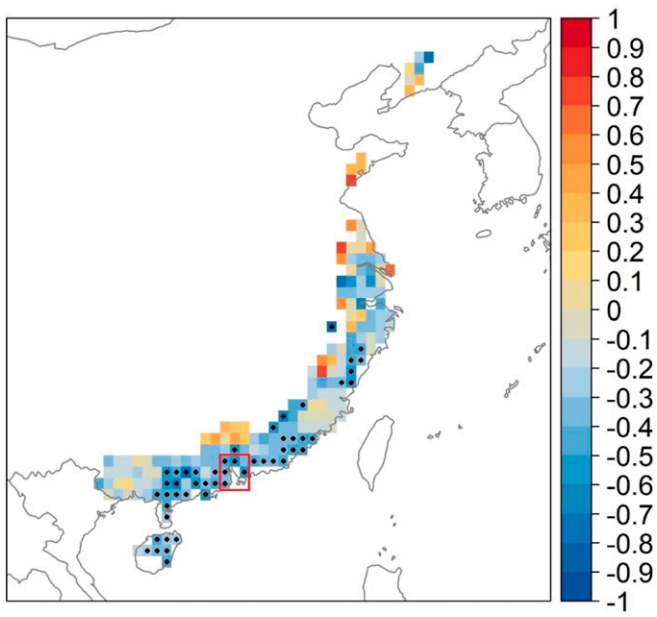
www.manaraa.com

Fig. 2. Spatial pattern of correlation coefficients of translation speeds and local rainfall totals of individual TCs over the coastal areas of China. Only TCs with rainfall intensity (mm/d) ≥ 30 mm/d and areas that have at least four TCs with rainfall intensity ≥ 30 mm/d are considered. Stippled regions represent areas with Spearman correlation coefficients significant at the 95% level. The red box indicates the location of the Pearl River Delta.

Furthermore, Fig. 3B shows that 10 out of 14 recorded TCs (marked with squares) with translation speed ≤ 15 km/h and rainfall intensity ≥ 30 mm/d occurred after 1990, and 3 of them produced rainfall totals of more than 200 mm in the Pearl River Delta, indicating a substantial increase of flood risks caused by TCs with low translation speeds in this region in recent years.

Finally, we compare the probability density functions (PDFs) and cumulative distribution functions (CDFs) of the local rainfall totals induced by slow- (≤ 15 km/h) and fast-moving (≥ 25 km/h) TCs and find that slow-moving TCs are more likely to generate high local rainfall totals (Fig. 4). The occurrence probabilities of local rainfall totals larger than 200 mm induced by slow-moving TCs are higher than those associated with fast-moving TCs. The PDF curve of rainfall totals of slow-moving TCs is wider than

that of fast-moving TCs, suggesting that slow-moving TCs may produce more extreme rainfall totals to a region as indicated by the longer and higher right tail. The CDF curves also show slow-moving TCs are more likely to generate higher local rainfall totals. The mean local rainfall totals of slow- and fast-moving TCs are 99.1 and 80.5 mm, respectively. In other words, slow-moving TCs produce about 20% more rainfall on average than fast-moving events.

Our work reveals that both the observed best-track data and the multimodel ensemble of CMIP5 GCMs suggest a significant slowdown of TCs (−0.044 km/h per year in observations and −0.038 km/h per year in simulations, respectively) over the coastal areas of China from 1961 to 2017. The agreement of the observations and simulations provides more confidence in the trend of TC slowdown. To explore the possible linkage between climate change and the trends of TC translation speed, we conduct a detection and attribution analysis using the optimal fingerprinting method (27–30) based on the historical simulations driven by ALL forcing (anthropogenic and natural radiative forcings) and NAT forcing (solar and volcanic combined), as well as preindustrial control runs of CSIRO-Mk3-6–0, the only CMIP5 GCM that provides complete 6-hourly outputs of these forcings and passes the residual consistency test (ref. 31 and *SI Appendix*, Appendix E). The detection result indicates that it is probable (90% significance level) that there is a climate change component associated with anthropogenic forcing in the observed TC slowdown. However, there are caveats arising from the effects of the uncertainties associated with GCMs on the detection result, and we consider further detection and attribution analyses based on multiple climate model simulations are necessary. In this study, we focus on the impacts of TC slowdown on local rainfall totals and our analyses show slower TCs tend to generate more rainfall over a given region. Specifically, as TC translation speeds decreased, the mean and the 90th percentile of TC-induced local rainfall totals exhibited increasing trends from 1961 to 2017. There are significant inverse correlations between local rainfall totals and TC translation speeds over the study period. The comparison of the PDFs of local rainfall totals induced by slow- and fast-moving TCs further indicate that slow-moving TCs are more likely to generate larger rainfall amounts. Therefore, this study highlights the evidence of TC slowdown in potentially elevating local rainfall totals and the associated greater flood risks, and therefore provides scientific support for better flood management and adaptation strategies in coastal regions under the threats of TCs.
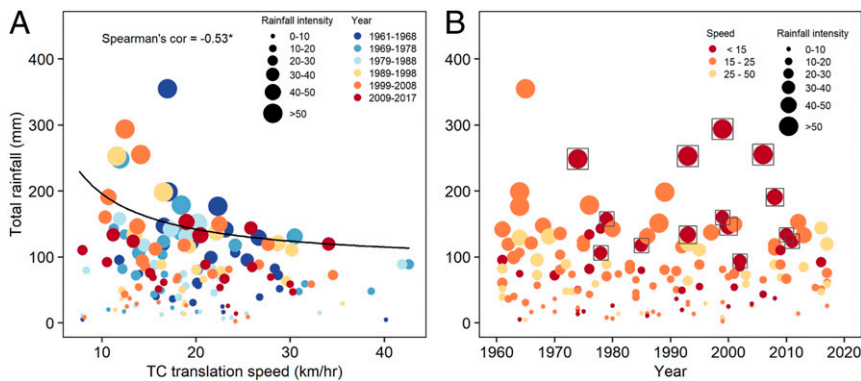
Fig. 3. Relationship of translation speed (km/h), local rainfall total (mm), rainfall intensity (mm/d), and year of occurrence of individual TC events that made landfall over the Pearl River Delta. (*A*) Scatter plot of translation speeds and local rainfall totals of individual TCs. (*B*) Temporal evolution of translation speeds and local rainfall totals of individual TCs. Size of circles indicates rainfall intensity. In *A*, colors indicate the years the TCs occurred, and in *B* colors indicate the translation speeds. The black curve shows that total rainfall is inversely proportional to translation speed for TCs with rainfall intensity ≥ 30 mm/d. The Spearman (−0.53) correlation coefficient of local rainfall totals and translation speed is calculated based on TCs with rainfall intensity ≥ 30 mm/d. "*" indicates the coefficient is significant at the 95% level. Squares in *B* highlight the TCs with translation speed ≤ 15 km/h and rainfall intensity ≥ 30 mm/d.
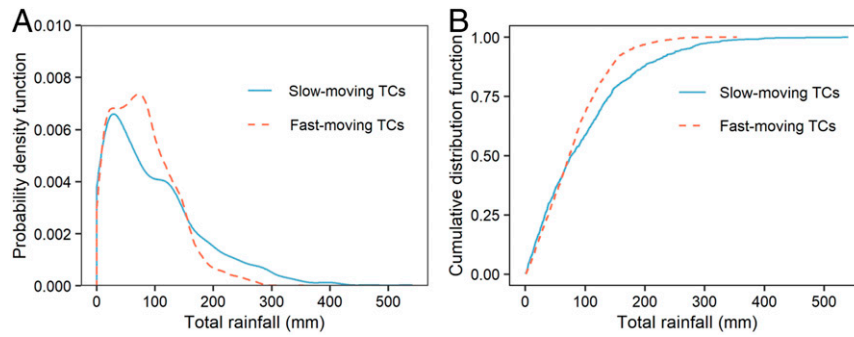
Lai et al.

www.manaraa.com

Fig. 4. Statistical distributions of local rainfall totals produced by slow-moving TCs (translation speed ≤ 15 km/h; blue) and fast-moving TCs (translation speed ≥ 25 km/h; red) in the coastal areas of China. (*A*) PDFs of local rainfall totals. (*B*) Cumulative distribution functions of local rainfall totals.

Methods

Estimation of TC Translation Speed. The study area is defined as the landside area within 200 km from the coastline of mainland China, because the contribution of a TC to rainfall decreases sharply as the distance from coastline increases. When the distance exceeds 200 km, the contribution drops below 10% (32, 33). Best-track data covering the western North Pacific during 1961–2017 are taken from the International Best Track Archive for Climate Stewardship (IBTrACS) archive (34). TC positions located within 200 km on both sides of the coastal study area are considered in this study. Translation speed is calculated by dividing the distance between every two neighboring positions along a TC track by the 6-hourly interval following ref. 1. The distance between track points is computed along a great circle arc. Over-land positions are determined using the 2-Minute Gridded Global Relief Data, a high-resolution global topography map (ref. 35 and see *Data Availability*). It should be noted that a translation speed is considered as over land whenever one track point is located on land and otherwise it is considered as over sea.

Identification and Tracking of TCs in GCM Simulations. TCs in CMIP5 GCMs are identified and tracked using the Camargo and Zebiak algorithm (36, 37). This algorithm is an objective method searching TCs in GCMs based on sea-level pressure, temperature at three pressure levels (850, 500, and 250 hPa), and winds at two pressure levels (850 and 250 hPa). In the CMIP5 archive, only GCMs with 6-hourly outputs of the above variables and with detected landfalling TCs in the study area in more than 30 y are selected. A total of eight GCMs, namely CSIRO-Mk3-6-0, GFDL-ESM2M, GFDL-CM3, HadGEM2-ES, MIROC5, MPI-ESM-LR, MRI-CGCM3, and NorESM1-M, are chosen for analyzing the changes in TC translation speed (*SI Appendix*, Table S1). The algorithm includes two parts: detection and tracking. In the detection part, potential TC points are identified based on four criteria: 1) relative vorticity at 850 hPa (ζ_{850}) exceeds the vorticity threshold (ζ_m); 2) maximum wind speed at 850 hPa exceeds the wind speed threshold (v_m); 3) vertically integrated local temperature anomaly exceeds the temperature anomaly threshold (T_m); and 4) genesis location locates in the tropics (30°S–30°N) over the ocean. Afterward, the potential TC points are connected by time if they are less than a certain distance that depends on the spatial resolution of model outputs. Only TCs lasting for more than 2 d are considered. In the tracking part, the first TC center is defined as the vorticity centroid of the vorticity matrix around the initial TC point identified in the detection part. The next TC center is the location of vorticity centroid in the next time step in nearby grid point. This process is repeated until the vorticity value is below a relaxed vorticity threshold (ζ_r) which is lower than the vorticity threshold value in the detection part. The tracking procedure is performed for each TC detected in the detection part. These thresholds are determined objectively by the joint probability distribution of these environmental variables in a given basin (western North Pacific for this study): the vorticity threshold is defined as twice the vorticity SD; the wind speed threshold is the sum of oceanic global wind speed and the SD of wind speed in each basin; the temperature anomaly threshold is calculated as the SD of integrated local anomalous temperature. The values of the four thresholds in the western North Pacific for the eight GCMs provided by Camargo (37) are listed in *SI Appendix*, Table S2.

Calculation of TC-Induced Rainfall. The observed gridded daily precipitation dataset of 1961–2017 at the 0.5° × 0.5° resolution is collected from the National Meteorological Information Center (NMIC) of China Meteorological

Administration (CMA; see *Data Availability*). This dataset was reproduced from the observations of 2,474 meteorological stations in China using the Thin Plate Spline method (38, 39). As suggested by ref. 33, TC-induced rainfall is defined as rainfall that occurs within 200 km of TC center from 1 d before to 1 d after the passage of a TC. Total rainfall of a TC in a given grid is the sum of rainfall amount in this grid (i.e., within 200 km from the TC center) during the whole period affected by this TC:

$$\text{Total rainfall} = \sum_{i=1}^{n} R_i, \qquad [1]$$

where n is the number of days on which the given grid is affected by the TC, and R_i is the rainfall amount (mm) in this grid on day i. The rainfall intensity in a given grid of a TC is calculated as follows:

$$I = \frac{\sum_{i=1}^{n} R_i}{n}, \qquad [2]$$

where I is the rainfall intensity (mm/d) of this TC in this grid.

Correlation Analysis. The correlation between TC translation speed and local total TC rainfall is estimated using Spearman and Pearson correlation coefficients (40, 41). The correlation coefficients are calculated for individual TC events. The increase of total rainfall amount is less sensitive to rainfall duration when rainfall intensity is low. Thus, only TCs with rainfall intensity ≥ 30 mm/d are considered for the calculation of correlation coefficient. In addition, only grids that have at least four passages of TCs (i.e., within 200 km of TC center) are considered in this study. The correlation coefficients based on TCs with rainfall intensity ≥ 10, 20, 40, and 50 mm/d are calculated to detect and verify the inverse relationships between TC translation speed and local rainfall total (*SI Appendix*, Appendix D).

Probability Distribution of Slow- and Fast-Moving TCs. Slow- and fast-moving TCs are defined as those with translation speed ≤ 15 km/h and ≥ 25 km/h, respectively, which are very close to the first and third quartile of the translation speeds of all TCs analyzed in this study. The differences between local rainfall caused by slow- and fast-moving TCs are examined by the two-sample Student's *t* test (42). Because weak TCs such as tropical depressions and tropical storms may bring limited rainfall but move slowly, those TCs with maximum wind speed < 65 kn are excluded when defining the slow- and fast-moving TCs in the probability analysis. The threshold of 65 kn is determined by the mean of maximum TC wind speed of the TCs analyzed.

Trend Detection. The significance of the trend in a time series is examined using the Modified Mann–Kendall test, a nonparametric trend detection method considering autocorrelation in time series (43). The magnitude of the trend in a time series is estimated using the Sen's slope method (44). The percentage change in the study period is calculated by dividing the difference between the values of the last year and the first year of the trend line by the value of the first year.

Data Availability. The tropical cyclone data in this study are collected from the International Best Track Archive for Climate Stewardship (IBTrACS; https://www.ncdc.noaa.gov/ibtracs/). TC track positions over land are determined based on the 2-Minute Gridded Global Relief Data (ETOPO2v2; https://www.ngdc.noaa.gov/mgg/global/etopo2.html). CMIP5 model outputs are available in the Earth System Grid Federation (ESGF) Peer-to-Peer system (https://esgf-node.llnl.gov/

www.manaraa.com

1. J. P. Kossin, A global slowdown of tropical-cyclone translation speed. *Nature* **558**, 104–107 (2018).
2. P. Peduzzi *et al.*, Global trends in tropical cyclone risk. *Nat. Clim. Chang.* **2**, 289–294 (2012).
3. W. Zhang, G. Villarini, G. A. Vecchi, J. A. Smith, Urbanization exacerbated the rainfall and flooding caused by hurricane Harvey in Houston. *Nature* **563**, 384–388 (2018).
4. F. C. Chien, H. C. Kuo, On the extreme rainfall of Typhoon Morakot (2009). *J. Geophys. Res. Atmos.* **116**, 1–22 (2011).
5. X. Chen, L. Wu, J. Zhang, Increasing duration of tropical cyclones over China. *Geophys. Res. Atmos.* **38**, 1–5 (2011).
6. C.-C. Wang *et al.*, Effects of asymmetric latent heating on typhoon movement crossing Taiwan: The case of Morakot (2009) with extreme rainfall. *J. Atmos. Sci.* **69**, 3172–3196 (2012).
7. T. M. Hall, J. P. Kossin, Hurricane stalling along the North American coast and implications for rainfall. *npj Clim. Atmos. Sci.* **2**, 1–9 (2019).
8. K. E. Trenberth, A. Dai, R. M. Rasmussen, D. B. Parsons, The changing character of precipitation. *Bull. Am. Meteorol. Soc.* **84**, 1205–1217 (2003).
9. G. Lenderink, E. van Meijgaard, Increase in hourly precipitation extremes beyond expectations from temperature changes. *Nat. Geosci.* **1**, 511–514 (2008).
10. T. R. Knutson *et al.*, Global projections of intense tropical cyclone activity for the late twenty-first century from dynamical downscaling of CMIP5/RCP4.5 scenarios. *J. Clim.* **28**, 7203–7224 (2015).
11. T. R. Knutson *et al.*, Dynamical downscaling projections of twenty-first-century atlantic hurricane activity: CMIP3 and CMIP5 model-based scenarios. *J. Clim.* **26**, 6591–6617 (2013).
12. C. M. Patricola, M. F. Wehner, Anthropogenic influences on major tropical cyclone events. *Nature* **563**, 339–346 (2018).
13. M. D. Risser, M. F. Wehner, Attributable human-induced changes in the likelihood and magnitude of the observed extreme precipitation during hurricane Harvey. *Geophys. Res. Lett.* **44**, 12,457-12,464 (2017).
14. K. Emanuel, Assessing the present and future probability of Hurricane Harvey's rainfall. *Proc. Natl. Acad. Sci. U.S.A.* **114**, 12681–12684 (2017).
15. J. P. Kossin, Reply to: Moon, I.-J. et al.; Lanzante, J. R. *Nature* **570**, E16–E22 (2019).
16. J. R. Lanzante, Uncertainties in tropical-cyclone translation speed. *Nature* **570**, E6–E15 (2019).
17. I. J. Moon, S. H. Kim, J. C. L. Chan, Climate change and tropical cyclone trend. *Nature* **570**, E3–E5 (2019).
18. M. Yamaguchi, J. C. L. Chan, I. J. Moon, K. Yoshida, R. Mizuta, Global warming changes tropical cyclone translation speed. *Nat. Commun.* **11**, 47 (2020).
19. G. Zhang, H. Murakami, T. R. Knutson, R. Mizuta, K. Yoshida, Tropical cyclone motion in a changing climate. *Sci. Adv.* **6**, eaaz7610 (2020).
20. E. Hawkins *et al.*, Uncertainties in the timing of unprecedented climates. *Nature* **511**, E3–E5 (2014).
21. K. E. Taylor, R. J. Stouffer, G. A. Meehl, An overview of CMIP5 and the experiment design. *Bull. Am. Meteorol. Soc.* **93**, 485–498 (2012).
22. L. Yang, J. Scheffran, H. Qin, Q. You, Climate-related flood risks and urban responses in the Pearl River Delta, China. *Reg. Environ. Change* **15**, 379–391 (2014).
23. Q. He *et al.*, Economic development and coastal ecosystem change in China. *Sci. Rep.* **4**, 5995 (2014).
24. M. Ying, B. Chen, G. Wu, Climate trends in tropical cyclone-induced wind and precipitation over mainland China. *Geophys. Res. Lett.* **38**, 1–5 (2011).
25. X. Wang *et al.*, Observed changes in precipitation extremes and effects of tropical cyclones in South China during 1955–2013. *Int. J. Climatol.* **39**, 2677–2684 (2019).
26. J. Zhang, L. Wu, F. Ren, X. Cui, Changes in tropical cyclone rainfall in China. *J. Meteorol. Soc. Jpn.* **91**, 585–595 (2013).
27. S.-K. Min, X. Zhang, F. W. Zwiers, G. C. Hegerl, Human contribution to more-intense precipitation extremes. *Nature* **470**, 378–381 (2011).
28. X. Gu *et al.*, Attribution of global soil moisture drying to human activities: A quantitative viewpoint. *Geophys. Res. Lett.* **46**, 2573–2582 (2019).
29. L. Gudmundsson, S. I. Seneviratne, X. Zhang, Anthropogenic climate change detected in European renewable freshwater resources. *Nat. Clim. Chang.* **7**, 813–816 (2017).
30. P. A. Stott, D. A. Stone, M. R. Allen, Human contribution to the European heatwave of 2003. *Nature* **432**, 610–614 (2004).
31. M. R. Allen, S. F. B. Tett, Checking for model consistency in optimal fingerprinting. *Clim. Dyn.* **15**, 419–434 (1999).
32. A. Khouakhi, G. Villarini, G. A. Vecchi, Contribution of tropical cyclones to rainfall at the global scale. *J. Clim.* **30**, 359–372 (2017).
33. Q. Zhang, Y. Lai, X. Gu, P. Shi, V. P. Singh, Tropical cyclonic rainfall in China: Changing properties, seasonality, and causes. *J. Geophys. Res. Atmos.* **123**, 4476–4489 (2018).
34. K. R. Knapp, M. C. Kruk, D. H. Levinson, H. J. Diamond, C. J. Neumann, The international best track archive for climate stewardship (IBTrACS) unifying tropical cyclone data. *Bull. Am. Meteorol. Soc.* **91**, 363–376 (2010).
35. National Geophysical Data Center, 2-minute gridded global relief data (ETOPO2v2). National Geophysical Data Center, NOAA. (2006). DOI: 10.7289/V5J1012Q. Accessed 9 February 2019.
36. S. J. Camargo, S. E. Zebiak, Improving the detection and tracking of tropical cyclones in atmospheric general circulation models. *Weather Forecast.* **17**, 1152–1162 (2002).
37. S. J. Camargo, Global and regional aspects of tropical cyclone activity in the CMIP5 models. *J. Clim.* **26**, 9880–9902 (2013).
38. M. F. Hutchinson, Interpolation of rainfall data with thin plate smoothing splines. Part I: Two dimensional smoothing of data with short range correlation. *J. Geogr. Inf. Decis. Anal.* **2**, 139–151 (1998).
39. M. F. Hutchinson, Interpolation of rainfall data with thin plate smoothing splines–Part II: Analysis of topographic dependence. *J. Geogr. Inf. Decis. Anal.* **2**, 152–167 (1998).
40. H. Myles, D. A. Wolfe, *Nonparametric Statistical Methods*, (Wiley, New York, 1973).
41. R. A. Fisher, *Statistical Methods for Research Workers*, (Oliver & Boyd, Edinburgh, ed. 5, 1934).
42. D. S. Wilks, *Statistical Methods in the Atmospheric Sciences*, (Elsevier, San Diego, 2011).
43. K. H. Hamed, A. Ramachandra Rao, A modified Mann-Kendall trend test for autocorrelated data. *J. Hydrol.* **204**, 182–196 (1998).
44. P. K. Sen, Estimates of the regression coefficient based on Kendall's Tau. *J. Am. Stat. Assoc.* **63**, 1379–1389 (1968).
45. Y. Sun, X. Zhang, G. Ren, F. W. Zwiers, T. Hu, Contribution of urbanization to warming in China. *Nat. Clim. Chang.* **6**, 706–709 (2016).
46. H. Chen, J. Sun, Contribution of human influence to increased daily precipitation extremes over China. *Geophys. Res. Lett.* **44**, 2436–2444 (2017).

EARTH, ATMOSPHERIC, AND PLANETARY SCIENCES

Lai et al.

www.manaraa.com